Response of the Jovian Magnetosphere-Ionosphere System to the Interplanetary Magnetic Field Discontinuity: A Simulation Study

Yuxian Wang, Xiaocheng Guo, Chi Wang, Michel Blanc

ADVANCING EARTH AND SPACE SCIENCE

JGR Space Physics

RESEARCH ARTICLE
10.1029/2021JA030207

Key Points:
- The response of the magnetosphere-ionosphere system to interplanetary magnetic field (IMF) discontinuities depends on local times and radial distances
- The magnetosphere and ionosphere significantly respond to the IMF discontinuity in 2–6 and 3–8 hr from the arrival at the bow shock
- We reproduce the upward field-aligned currents with a general morphology in accord with the observed ultraviolet main auroral ovals for the first time

Supporting Information:
Supporting Information may be found in the online version of this article.

Correspondence to:
X. Guo and C. Wang,
xcguo@spaceweather.ac.cn;
cw@spaceweather.ac.cn

Citation:
Wang, Y., Guo, X., Wang, C., & Blanc, M. (2022). Response of the Jovian magnetosphere-ionosphere system to the interplanetary magnetic field discontinuity: A simulation study. *Journal of Geophysical Research: Space Physics*, *127*, e2021JA030207. https://doi.org/10.1029/2021JA030207

Received 10 DEC 2021
Accepted 14 MAY 2022

Response of the Jovian Magnetosphere-Ionosphere System to the Interplanetary Magnetic Field Discontinuity: A Simulation Study

Yuxian Wang[1,2], Xiaocheng Guo[1,2], Chi Wang[1,2], and Michel Blanc[3]

[1]State Key Laboratory of Space Weather, National Space Science Center, Chinese Academy of Sciences, Beijing, China, [2]College of Earth and Planetary Sciences, University of Chinese Academy of Sciences, Beijing, China, [3]Institut de Recherche en Astrophysique et Planétologie, Toulouse, France

Abstract The response of the magnetosphere-ionosphere (MI) system at Jupiter to the interplanetary magnetic field (IMF) tangential discontinuity is studied via global Magnetohydrodynamics (MHD) simulations. Our results show that the IMF discontinuity, which has a transition front perpendicular to the Sun-Jupiter line, has strong effects on the Jovian MI system depending on local times and radial distances to Jupiter. The magnetospheric significant response to the discontinuity is delayed by ~2–6 hr after the encounter of the discontinuity front with the bow shock, while the delay time for the ionospheric field-aligned currents (FACs) is ~3–8 hr. The outer magnetosphere, particularly at dayside, tends to respond slightly quicker than the inner regions. At the ionosphere, the response of downward FACs is found to occur earlier than that of the upward ones by a time ranging from less than 1 hr to several hours, which is also more prominent at dayside sectors. Using a new MI mapping method with Jupiter's JRM09 magnetic field model, we reproduce for the first time the ionospheric FACs consistent with the morphology of the observed ultraviolet (UV) main auroral emissions. This indicates a potential application of the simulated upward FACs on the morphology of the UV main auroral ovals.

Plain Language Summary Jupiter's magnetosphere is driven mainly by the planet's fast rotation and the solar wind. Auroral observations have confirmed that the solar wind significantly modulates the magnetosphere-ionosphere (MI) system. Due to the enormous size of the magnetosphere and the interplay of the planet's fast rotation and the solar wind, the responses of the Jovian magnetosphere and ionosphere to the solar wind are expected to be very different from those observed at Earth. In this article, we use magnetohydrodynamics simulations to investigate the response of the MI system to the interplanetary magnetic field rotations. We also use a realistic Jupiter's planetary magnetic field in our simulations to calculate the ionospheric currents, so as to examine the effects of the planetary magnetic field on the shaping of the ionospheric currents and main auroral emissions.

1. Introduction

1.1. The Interaction of the Solar Wind With the Jovian Magnetosphere

The interaction of the solar wind with planetary magnetospheres is one of the hot topics in space physics. While the Jovian magnetosphere is known to be largely controlled by internal mechanisms associated with the planet's fast rotation (~10 hr) and the Iogenic plasma source (Khurana et al., 2004; Krupp et al., 2004), the role of the solar wind in Jovian magnetospheric dynamics remains an open issue (Bagenal et al., 2017), due in part to insufficient in situ observations of the magnetosphere and the absence of an upstream solar wind monitor. However, there are many processes by which the solar wind can influence the Jovian MI system, such as the magnetopause boundary processes, which include the motion of the magnetopause, magnetic field reconnection and Kelvin-Helmholtz instability (e.g., Delamere et al., 2015 and references therein).

In addition, auroral observations also provide important clues for the solar wind influence. Observations have confirmed that the solar wind significantly modulates the auroral emissions in multiple wavebands such as UV (Clarke et al., 2009) and X-ray emissions (Dunn et al., 2016, 2020). Clarke et al. (2009) suggested that the UV main emission brightens and thickens in response to solar wind shocks, while an expanded magnetosphere leads the main emission to dim (Badman et al., 2016). This conclusion is consistent with the Magnetohydrodynamics

(MHD) simulations by Chané et al. (2017), who found that the upward ionospheric FACs, which were used as a proxy of main emission, are positively correlated with the solar wind ram pressure, and the local time asymmetries in the magnetosphere are also enhanced when the ram pressure increases.

Global MHD models are widely used to investigate the large-scale dynamics of the Jovian magnetosphere (Chané et al., 2013, 2017; Fukazawa et al., 2005, 2006; Joy et al., 2002; Sarkango et al., 2019; Tanaka et al., 2021; Y. X. Wang et al., 2018; Zhang et al., 2018, 2021 and references therein). However, among these models, only a few of them were employed to study the response of the MI system to solar wind discontinuities such as tangential discontinuities and shocks. Instead, most models were used for studies under idealized steady solar wind conditions (e.g., Y. X. Wang et al., 2018; Zhang et al., 2018). Using the BATSRUS MHD code, Sarkango et al. (2019) conducted a series of simulations with various types of changes in the upstream solar wind, such as an IMF discontinuity (also referred to as IMF rotation hereafter) and a dynamic pressure enhancement. They found that a south-to-east IMF discontinuity has a significant impact on the large-scale current system, while the response of the MI system to the shock is even more dramatic. Unfortunately, to date, all these Jovian MHD models use a simple axisymmetric dipole for the planetary magnetic field, with or without a tilt angle between the magnetic axis and the rotational axis. As a matter of fact, Jupiter's intrinsic magnetic field as observed by in situ measurements exhibits extraordinary hemispheric asymmetry and significant anomalies, especially in the northern polar region (Connerney et al., 2018). If these features of the real Jovian magnetic field are not taken into account, the simulated ionospheric FACs and thus the indicated main ovals are always circular around the magnetic axis and are almost symmetric between northern and southern poles (e.g., Sarkango et al., 2019; Tanaka et al., 2021; Y. X. Wang et al., 2018), which deviate significantly from the observations (Grodent et al., 2018 and references therein).

1.2. Introduction to Jupiter's Aurora and Its Main Oval

The UV aurora consists of three main components with almost equal power (Grodent et al., 2018): (a) the relatively stable main auroral emissions; (b) the variable emissions poleward of the main oval, and (c) the equatorward emissions including diffuse, patchy and sometimes arc-like auroral emissions as well as satellite footprints. The main emissions are magnetically mapped to 20–60 R_J near the equator (Vogt et al., 2011). It is generally accepted that they correspond to the upward ionospheric FACs predicted by the corotation enforcement theory (Cowley & Bunce, 2001; Hill, 2001; Nichols & Cowley, 2004; Southwood & Kivelson, 2001). In this theoretical framework, the radial currents flowing within the magnetodisk accelerate the subcorotating plasma via the Lorentz force to maintain it in partial corotation. These currents then diverge into FACs connecting the magnetosphere and ionosphere, which finally close through the ionosphere as Pedersen currents. At the ionospheric level, the downward FACs are distributed at higher latitudes and extend to the pole, while equatorward of them, the upward FACs form a narrow latitudinal band centered around 15° magnetic colatitude. These upward FACs are expected to peak at a latitude mapping to the equatorial magnetosphere where corotation breakdown occurs (e.g., Cowley & Bunce, 2001). The idea of such global current system and its relation to the main oval provides a possible explanation for some observations such as the discontinuity located at the prenoon sector (Radioti et al., 2008), and the subcorotation in the ionosphere along with the rotating magnetosphere, indicative of the momentum and energy transfer between the magnetosphere and ionosphere, derived by Y. X. Wang, Blanc, et al. (2021) from Juno multi-instrument data analysis and modeling. Interestingly, this large-scale current system including the ionospheric FACs and equatorial radial directed currents, the discontinuity in the main aurora and the plasma flow in the magnetosphere and ionosphere are well reproduced by MHD models (e.g., Chané et al., 2013; Sarkango et al., 2019; Tanaka et al., 2021; Y. X. Wang et al., 2018).

However, Bonfond et al. (2020) pointed out several contradictions between the predictions of this corotation enforcement theory and observations. For instance, the observed main aurora brightens with higher solar wind ram pressure (e.g., Badman et al., 2016; Clarke et al., 2009), which is opposite to the predictions of the corotation enforcement theory. Another observation challenging the corotation enforcement theory is that stochastic acceleration processes are observed to prevail over quasi-electrostatic potential drops in particle acceleration over a large fraction of the main aurora at Jupiter, contrary to what is observed at Earth (Mauk et al., 2018). Thus, the links between the main oval and the upward ionospheric FACs are not always firm or reliable. In addition, the UV aurora is essentially solely related to the characteristic energy and fluxes of precipitating electrons (regardless of upward electrons), which is not a reliable proxy for the net upward FACs, and vice versa. It is noteworthy that our present study does not rely on the corotation enforcement theory, except for the assumption that the upward ionospheric FACs are as a proxy for the main auroral morphology, which is a more relaxed assumption, which is widely used in MHD simulations (e.g., Chané et al., 2017, 2013; Sarkango et al., 2019; Tanaka et al., 2021; Y. X. Wang et al., 2018).

1.3. Objective of This Study and Organization of the Paper

As described in Section 1.1, it is still poorly understood how the Jupiter system responds to the solar wind, and in particular few studies have been implemented to investigate the response of the MI system to the solar wind discontinuities. In addition, the morphology of the simulated main ovals significantly deviates from observations for all previous MHD models. In the present study, we perform a series of simulation runs in order to investigate how the MI system responds to the IMF rotations particularly at the early stage. Our main goal is to evaluate the time delays between the time when the IMF discontinuity encounters the bow shock and the time when the MI system starts to experience significant changes at different local times and radial distances. Furthermore, we also examine the effects of the planetary magnetic field on the derived ionospheric FACs by adopting different MI mapping methods.

The paper is organized as follows. Our MHD model is described in Section 2. The main results are presented in Section 3 and discussed in Section 4. We conclude this paper with a summary in Section 5.

2. Model Description

The MHD model used in this study for the Jovian global magnetosphere was developed by Y. X. Wang et al. (2018), which incorporates mass loading from Jupiter's volcanic satellite Io, the planet's fast rotation, and the electrostatic coupling between the magnetosphere and ionosphere. Only one ion species, namely protons, is considered in our one-fluid MHD model. A more detailed description of the model can be found in Y. X. Wang et al. (2018). Here, we only review some aspects of the model involved in this study, including the numerical domain, the MI coupling method, and the upstream solar wind inputs.

2.1. Numerical Domain

The model takes a Jupiter-centered Cartesian coordinate system, which is inertially fixed with respect to an x-axis pointing to the Sun. The z-axis is along the Jupiter rotation axis (+z for northward) and the y-axis completes the right-handed system. The simulation domain is taken to be $-500\ R_J \leq x \leq 150\ R_J$, $-500\ R_J \leq y, z \leq 500\ R_J$ with comparable grid resolution relative to Y. X. Wang et al. (2018). The grids are smallest at the inner boundary ($r = 5.0\ R_J$), with a size of 0.6 R_J, and biggest, 7.9 R_J, at the outer boundary around 500 R_J.

2.2. Magnetosphere-Ionosphere Coupling Method

The MI coupling processes in Jovian MHD models are always greatly simplified under a quasi-static approximation (e.g., Y. X. Wang et al., 2018; Sarkango et al., 2019). As shown in Figure 1, MI coupling processes are described in the spherical shell region extending from the ionosphere (blue circle) to the inner boundary of the simulation domain (green circle), where the ionosphere and magnetosphere are connected via magnetic field lines. As a result, the effect of the ionosphere is treated as a boundary condition, using the assumption that the perturbations of the FACs at the inner boundary (~5 R_J) propagate instantaneously to the ionosphere at 1 R_J. This assumption, widely used in MHD models, is justified by the fact that Alfvén travel times between the green and blue boundaries are very small compared to characteristic flow times (e.g., Sarkango et al., 2019; Y. X. Wang et al., 2018; Yu & Ridley, 2009).

Figure 2 shows the main steps of the MI coupling method in each coupling loop: (a) the FACs at the inner boundary of the MHD simulation are mapped along the magnetic field to the ionosphere at ~1 R_J; (b) the electric potential is solved in the two-dimensional ionospheric shell with prescribed Pedersen and Hall conductances; (c) then the ionospheric electric field and potential are mapped back to the inner boundary; and (d) they are used to drive the plasma EXB convection (see Y. X. Wang et al. [2018] for more details). Until now, all the MHD models for Jovian magnetosphere employ a dipole magnetic field for the mapping between the magnetosphere

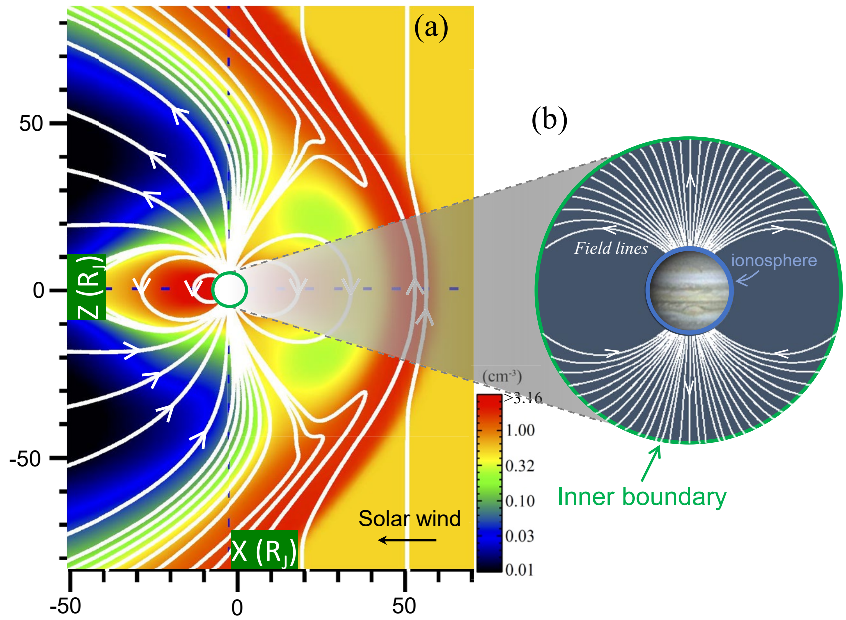

Figure 1. Schematic illustration of the magnetosphere-ionosphere coupling method. (a) The simulated Jovian magnetosphere under the northward interplanetary magnetic field condition on the noon-midnight meridian plane (*xz* plane). The background color contours the number density in log scale. The white curves indicate the magnetic field lines and the green circle represents the inner boundary at 5 R_J. (b) A close-up of the inner boundary illustrating the mapping between the magnetosphere, that is, inner boundary, and the ionosphere (blue circle) via magnetic field lines.

and ionosphere (see Section 1.1), which is the root cause for the discrepancy on the main oval morphology between the simulations and observations. As a first attempt to address this issue and to incorporate more realistic and complicated factors in the MI coupling, we adopt three different mapping methods: (a) a dipole field, (b) the JRM09 model, and (c) the JRM09 model plus a tilt angle correction (the left column in Figure 2). The Jovian planetary magnetic field is well described by the JRM09 model, which was obtained from Juno observations (Connerney et al., 2018). It is noteworthy that the JRM09 model has not been included in the MI coupling

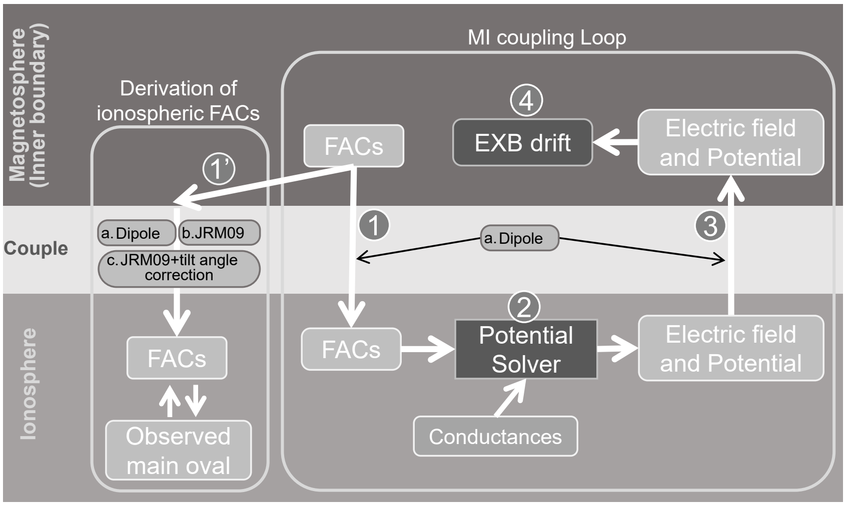

Figure 2. Logic diagram of the magnetosphere-ionosphere (MI) coupling method and different mapping methods to derive the ionospheric field-aligned currents (FACs). The numbers 1–4 indicate the calculation steps in each MI coupling loop, while the number 1' in the left column represents the procedure to derive the FACs with three different mapping methods: (a) a dipole field, (b) the JRM09 model, and (c) the JRM09 model plus a tilt angle correction. The newly derived FACs are then compared with the observed main ovals.

10.1029/2021JA030207

Table 1
Upstream IMF Conditions and Initial Magnetospheric States for the Simulations

Simulation Runs	New IMF directions	Initial magnetosphere	Changes in IMF (nT)
Run 1 Southward IMF + quasi-steady magnetosphere (under northward IMF)	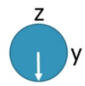	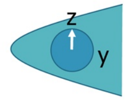	(0, 0, 0.5) → (0, 0, -0.5)
Run 2 Eastward IMF + quasi-steady magnetosphere (under northward IMF)	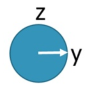	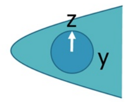	(0, 0, 0.5) → (0, 0.5, 0)
Run 3 Northward IMF + quasi-steady magnetosphere (under southward IMF)	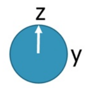	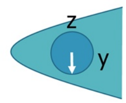	(0, 0, -0.5) → (0, 0, 0.5)

loop yet, but is only used to map the ionospheric FACs down and up between the green and blue boundaries of Figure 1. Therefore, the effects of the real planetary magnetic field, represented by the JRM09 model, on the MI coupling, in particular the tilt angle (~10.31°) of the magnetic axis relative to the rotational axis, are not included in the MHD simulation. Eventually, we used a minor modification to the modeled main oval, referred hereafter as the tilt angle correction, to compensate for the tilt angle effects on the MI system, which are not included in our current model. Note that the tilt angle and associated dipole magnetic axis mentioned here refer to the dipole approximation to the Jovian magnetic field based on the JRM09 model (Connerney et al., 2018).

2.3. The Upstream Solar Wind

In this study, we have performed three simulation runs with different IMF discontinuities and varying initial magnetospheric states. The input to the model is simply a step function of B_y or B_z (column 4 of Table 1), while other solar wind parameters remain constant: solar wind density $n = 0.5$ cm^{-3}, velocity $V_x = -400$ km/s, $V_y = V_z = 0$, magnetic field $|B| = 0.5$ nT, $B_x = 0$, and temperature $T = 60000$ K. In order to minimize the effects of initial magnetospheric transients, we first create a quasi-steady magnetosphere by using a constant solar wind with purely northward (Runs 1 and 2) or southward (Run 3) IMF. Then an IMF discontinuity is introduced at the upstream boundary to interact with the magnetosphere until a new quasi-steady state is reached.

Following the procedures as described above, as shown in Table 1, we first run the simulation with a north-to-south IMF turning interacting with a quasi-steady magnetosphere under northward IMF conditions. To investigate the effects of different IMF rotations, we then perform Run 2 with a north-to-east IMF turning. Finally, Run 3 is simulated with a south-to-north IMF turning interacting with an initial magnetosphere under a southward IMF.

3. Simulation Results

In this section, we present simulation results of the interaction of different IMF rotations with the magnetosphere. In the following sections, we first show the results for the ionospheric FACs morphology derived with the three different mapping methods described in Section 2.2. Then we analyze the response of the MI system to the solar wind discontinuity by taking the FACs and the thermal pressure P as proxies for the ionosphere and magnetosphere, respectively. Since the main focus of this study is on the relative time delays in the response of the MI system to the IMF discontinuity at different sectors and radial distances, the selection of proxies does not affect our main conclusions because different magnetospheric plasma parameters nearly simultaneously respond during the solar wind interactions.

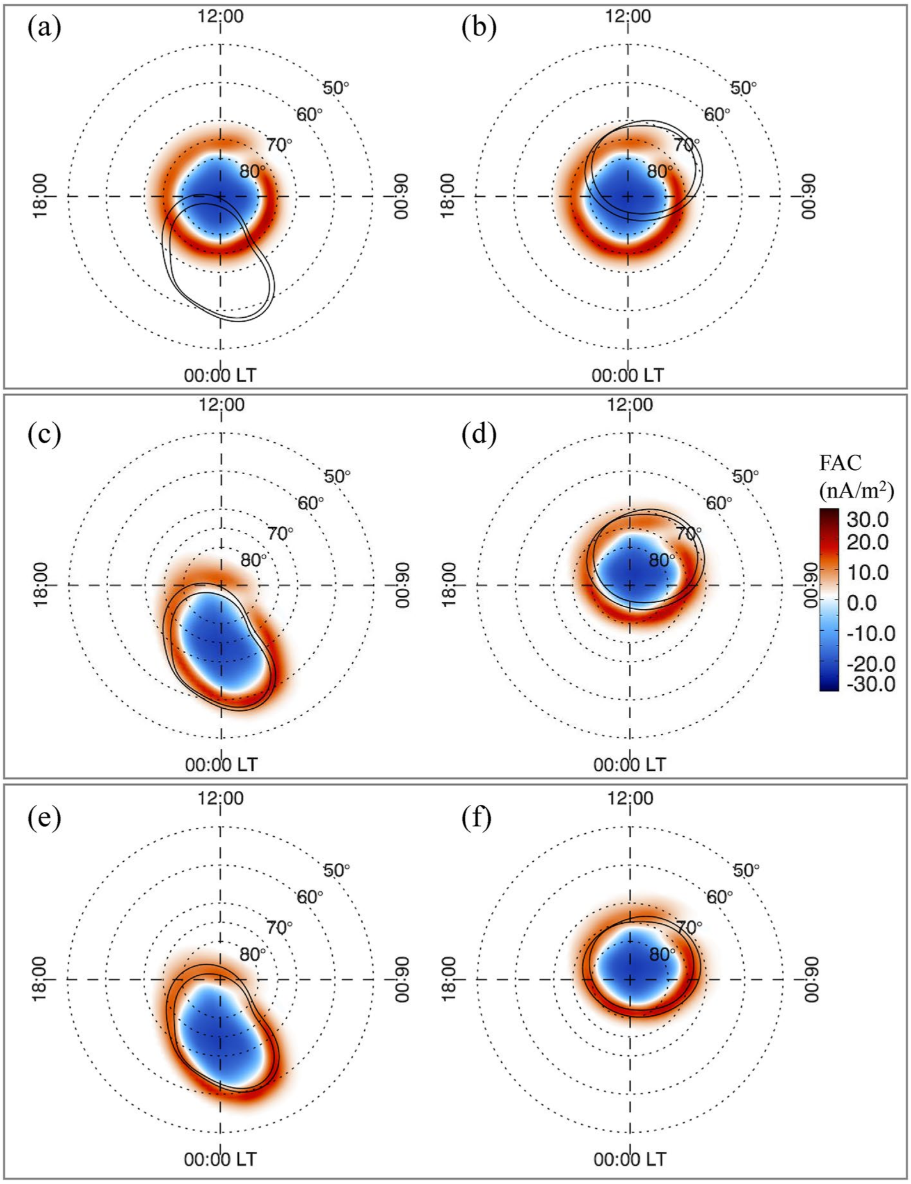

Figure 3. The Northern (left column) and Southern (right column) ionospheric field-aligned currents (FACs) in the SM coordinates calculated with different mapping methods: (a and b) zero-tilted dipole magnetic field, (c and d) JRM09 model, and (e and f) JRM09 model plus a tilt angle correction. The statistical main ovals adapted from Bonfond et al. (2012) are plotted with black curves for each panel. Positive values of FACs represent upward currents (in red), while negative values mean downward currents (in blue). The local times and latitudes are depicted on each panel. The Sun is to the top.

3.1. Morphology of Ionospheric FACs

Figure 3 shows the ionospheric FACs calculated with different mapping methods at a time when the 0° System III longitude aligns with the *x*-axis of SM coordinates, during which the magnetosphere reaches its steady state under a northward IMF condition. In the three runs presented in this study, the general morphology of the FACs, that is, their basic structure and configuration, is not significantly changed, although the value of the FACs changes in response to the solar wind discontinuity, as will be discussed in detail in Section 3.2. Therefore, the ionospheric FACs shown in Figure 3 are representative of the morphology obtained for the three runs.

It can be seen from Figure 3 that the morphology of simulated FACs differs significantly for different mapping methods. Similar to the results from preexisting Jovian MHD models (e.g., Sarkango et al., 2019; Tanaka et al., 2021; Y. X. Wang et al., 2018), the FACs in northern and southern hemispheres appear symmetric and are both circular around the magnetic axis for the dipole mapping method (see Figures 3a and 3b). However, such morphology deviates from the observations of the main oval as indicated with black curves, which show strong north-south asymmetries and equatorward shifting. As shown in Figures 3c and 3d, with a more realistic planetary magnetic field, that is, JRM09 model, used in the mapping procedure, the derived ionospheric FACs are greatly improved for both hemispheres. The resultant morphology of the upward FACs is basically in agreement with observations, although there is some shift between them. The simulated upward FACs reproduce the kink and non-circular pattern of the northern hemisphere and also the near circular southern pattern similar to observations. As mentioned in Section 2.2, the tilted JRM09 model is not implemented in the MI coupling loop (Figure 2); thus, a correction on the tilt angle is needed for the derivation of the FACs. Figures 3e and 3f show the results after the tilt angle correction, where the statistical main ovals are shifted toward the rotational axis by ∼3.6°. Note that this correction angle, that is, 3.6°, is smaller than the tilt angle of ∼10.31° of the dipole component of Jupiter's planetary magnetic field with respect to the geographic poles, which implies that the tilt angle influence on MI coupling may be somehow weakened. As a result, the morphology of the simulated upward FACs agrees quite well with observations, in terms of both outlines and locations.

3.2. The Response of the Magnetosphere-Ionosphere System

As described in Section 2.3, three runs with different IMF rotations are simulated to investigate the response of the MI system. In this section, we aim to analyze the characteristic time delays between the times when the IMF discontinuity encounters the bow shock and when the MI system begins to significantly respond. In the following, we first give an overview of the main features of the MI system response to the IMF discontinuity for Run 1. Then we discuss the ionospheric response in terms of the FACs in Section 3.2.2 and the magnetospheric response in Section 3.2.3.

3.2.1. Overview of the Magnetosphere-Ionosphere System Response

Taking Run 1 as an example, Figures 4c–4h show the time series of residual total upward and downward FACs at the ionospheric level (Figures 4c and 4d) and the magnetospheric thermal pressure at different radial distances (Figures 4e–4h). The residual currents and pressure are obtained by removing the values at 00:00 UT (or 0 hr), when the MI system is not disturbed by the solar wind discontinuity. Note that the total upward ionospheric current at each hemisphere amounts to about 8.5 MA (not shown here), which is comparable to or somewhat lower than the values obtained from Juno data, indicating an upward current system for the northern hemisphere ranging from ∼6 to ∼62 MA, and for the southern one varying from ∼26 to ∼91 MA (Kotsiaros et al., 2019). As defined in Figure 4a for the ionosphere and Figure 4b for the magnetosphere, for convenience of comparison between different local times, the MI system is separated into four sectors according to local times (LT): (a) 12:00–18:00 LT, (b) 18:00–24:00 LT, (c) 00:00–06:00 LT, and (d) 06:00–12:00 LT corresponding to an azimuthal angle (φ) increasing from 0 to 360°. It is noteworthy that each of the four sectors of the ionosphere covers the whole hemisphere with latitudes ranging from 0 to 90°, while that for the magnetosphere covers an infinitely thin arc on the equatorial plane at a specific radial distance (r). The ionospheric FACs are calculated with the dipole mapping method as shown in Figure 2. Since the magnetospheres simulated in this study are highly compressed, here we only focus on magnetospheric regions within 40 R_J, so as to eliminate the effects of the magnetopause (∼45 R_J) and its outside magnetosheath.

The tangential discontinuity front travels at the solar wind speed before it impacts the bow shock and is subsequently slowed down in the magnetosheath. For Run 1 studied in this paper, the IMF rotation transition front encounters the bow shock at around 03:35 UT (or 3.58 hr in Figure 4) at a solar wind speed of 400 km/s, where the 00:00 UT (or 0 hr) represents the time when the discontinuity is introduced at the upstream boundary. At the beginning, the MI system is under northward IMF conditions, corresponding to an open magnetosphere created due to dayside magnetic reconnection.

Figure 5 shows a close-up of Figures 4c–4h from 2 to 10 hr after 00:00 UT for Run 1 (see Figures S2 and S5 in Supporting Information S1 for Runs 2 and 3, respectively). One can see in this figure that a package of perturbations take place before the significant changes of the MI system shown with gray shadings. Here, the start times when the MI system significantly responds after the perturbations are determined by locating the immediate neighboring extrema, after which the FAC (or pressure) goes far beyond zero, that is, the initial state (see more clearly in Figure 4). This method is efficient for removing the effects of the small-scale perturbations and is

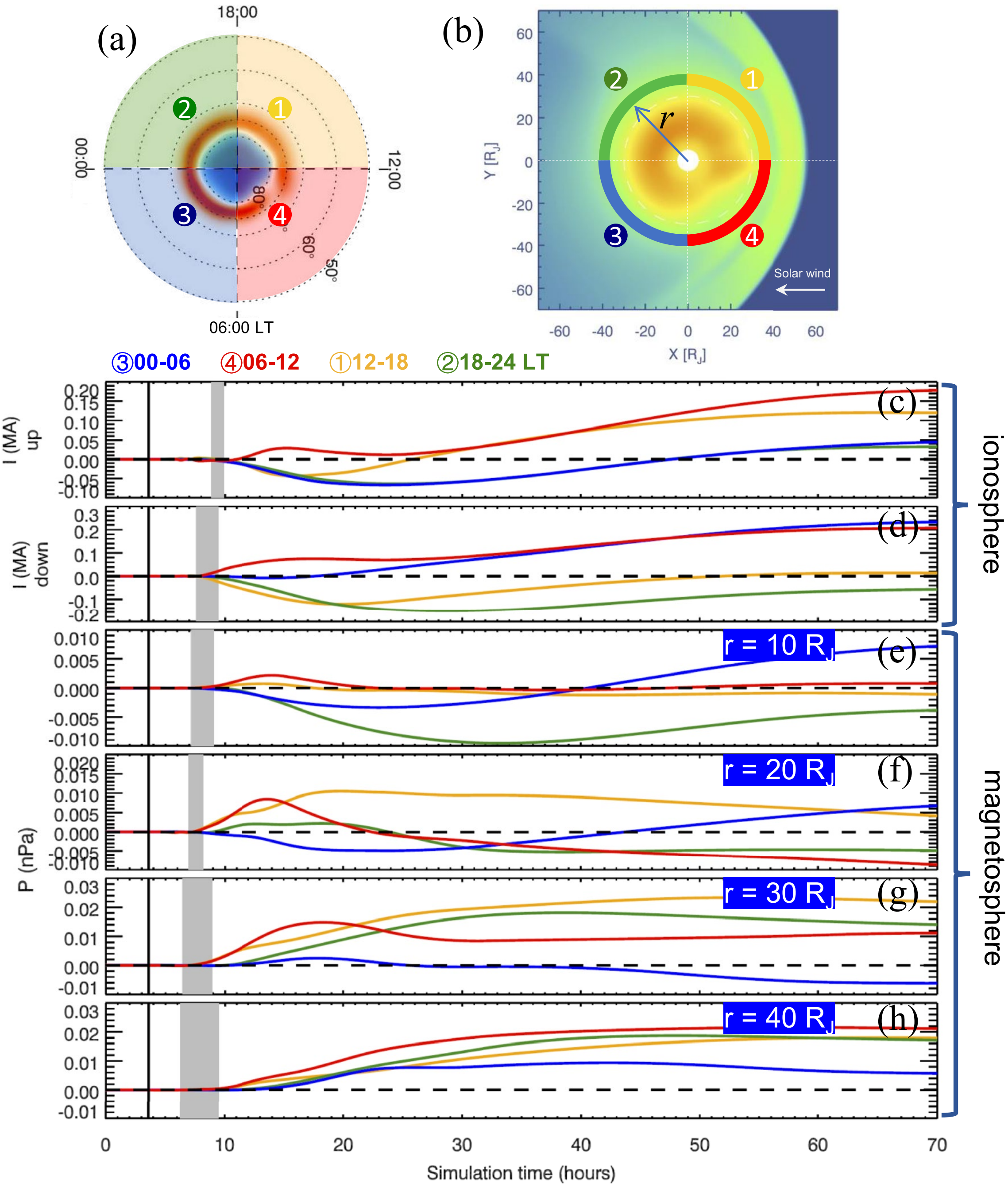

Figure 4. The residual total ionospheric field-aligned current (Figures 4c and 4d) and magnetospheric thermal pressure (Figures 4e–4h) relative to the initial state for Run 1 as a function of the simulation time. The 0 hr corresponds to the time when the IMF discontinuity is introduced at the upstream boundary. The colors in Figures 4c–4h represent the four sectors: 00:00–06:00 (blue), 06:00–12:00 (red), 12:00–18:00 (orange) and 18:00–24:00 LT (green) as defined in Figures 4a and 4b for the ionosphere and magnetosphere, respectively. Note that the ionosphere and magnetosphere shown in Figures 4a and 4b are only used to illustrate the definitions of the four sectors, but they do not represent any state of the magnetosphere-ionosphere (MI) system for Run 1. The Sun is to the right in Figures 4a and 4b. The black vertical solid lines in Figures 4c–4h indicate the time when the discontinuity encounters the bow shock. The times when the parameters of the MI system at different LT sectors starts to significantly change are covered by gray shadings in the corresponding panel.

universal for all situations in this study. At around 04:00 UT (4.0 hr), the dayside outer magnetosphere at 40 R_J begins to be perturbed with amplitudes below 0.1% of the background. Later, fluctuations propagate inward in sequence, until they reach the 10 R_J radial distance at 04:50 UT (4.83 hr). During this time period, at around 04:45 UT (4.33 hr), the ionospheric FACs start to fluctuate with a small amplitude of less than 2% of the background,

10.1029/2021JA030207

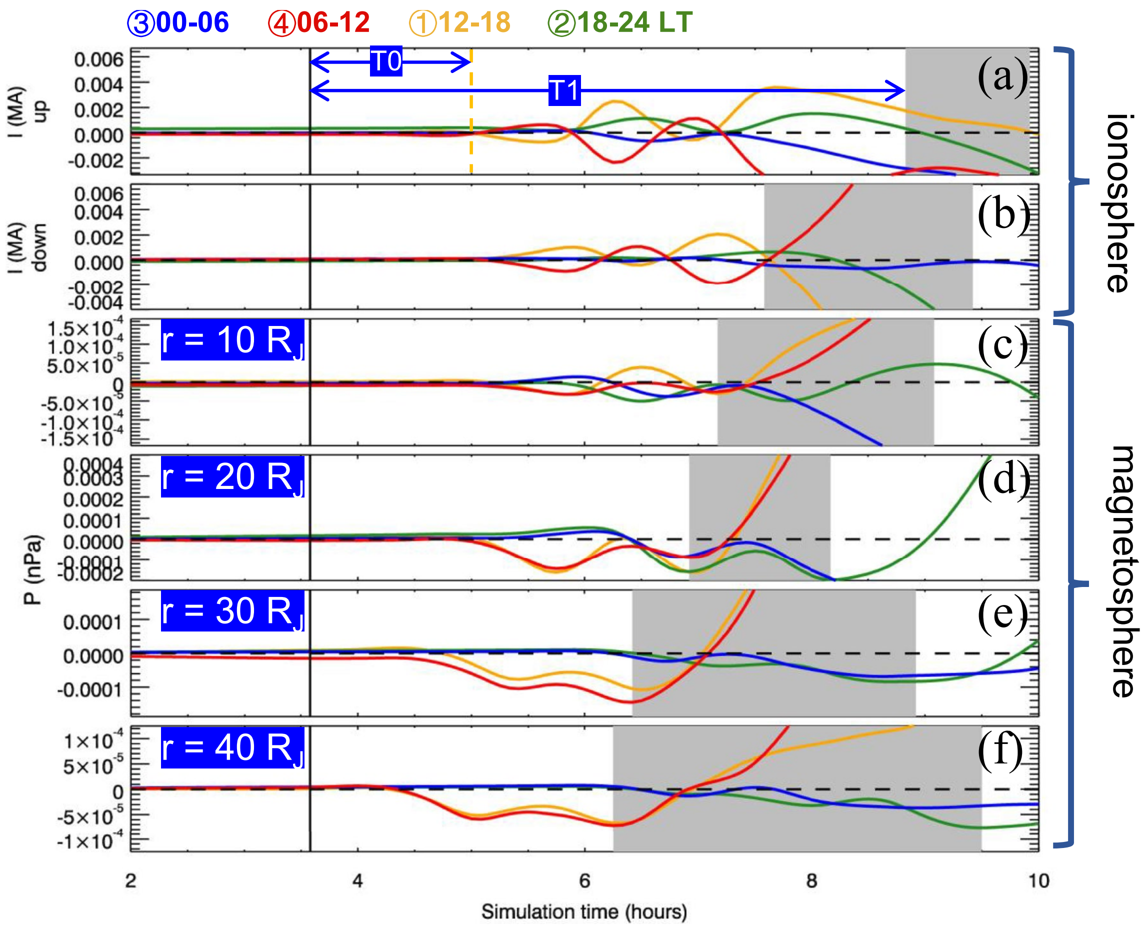

Figure 5. Same format as Figures 4c–4h, but with an interval from 2 to 10 hr for simulation time. The definitions of T0 and T1 are illustrated in Figure 5a.

implying the IMF discontinuity disturbs the ionospheric current system, until about 07:35 UT (7.58 hr) when the downward FACs significantly change (Figure 5b). Similarly, the magnetospheric fluctuations last until around 06:15 UT (6.25 hr) when the outer magnetosphere dramatically responds, indicating that the IMF rotation begins to effectively influence the MI system. The MI system takes over 70 hr to gradually reach another steady state.

3.2.2. Ionospheric Response

As one can see in Figures 4c and 4d, the response of the ionosphere to the IMF discontinuity shows significant local time asymmetries in terms of both magnitudes and general trends. For example, the upward FACs shown in Figure 4c in the prenoon dayside sector, that is, sector 4, tend to increase at the early stage after the encounter of IMF transition with the bow shock, reaching a local peak, which is followed by a gradual enhancement until a new steady state is reached. In contrast, the FACs at other sectors gradually decrease with similar slopes at first, and then gradually increase until a new state is reached after a local valley. Note that sector 4 is colocated with the main oval discontinuity (see Figure 4a). Besides, the FACs in sectors 1 and 4 seem to be anticorrelated at the early stage before ~20:00 UT (20 hr), that is, the duskside FACs at sector 1 tend to decrease, while the dawnside ones in sector 4 increase with comparable magnitudes. This anticorrelation can be found in all the three runs presented in this study, although the time evolutions of the FACs are quite different. For Runs 1 and 2, the general trends of the FACs in sectors 1 and 4 are similar, that is, increasing at the dawnside (sector 4) and decreasing at the duskside (sector 1) (see Figures 4c–4d and Figures S1c–S1d in Supporting Information S1). However, for Run 3, the dawnside FACs are weakened while the duskside FACs increase, opposite to Runs 1 and 2 (see Figures S4c–S4d in Supporting Information S1). This may be explained by the expansion or compression of the magnetosphere. Runs 1 and 2 have the same initial magnetosphere under northward IMF; thus, the interaction with the new upstream southward or eastward IMF brought by the IMF rotation results in a less compressed magnetosphere with decreasing open magnetic fluxes. As opposed to Runs 1 and 2, Run 3 simulates the northward IMF interacting with an initial magnetosphere under a southward IMF, producing more open flux and a more compressed magnetosphere. This is consistent with the simulation results from Chané et al. (2017), showing that for a more compressed magnetosphere, the total brightness of the main oval increases while the main oval near the discontinuity becomes fainter (see Figure 7 of Chané et al., 2017). It should be noted that the compression of the magnetosphere in Chané et al. (2017) was caused by the increased solar wind dynamic pressure instead of the IMF as in this study.

In addition to the local time asymmetries, the responses of the upward and downward FACs are quite different. First, as shown in Figure 4c, the responses of the upward FACs in the nightside sectors 2 and 3 are nearly identical, while those of the dayside sectors 1 and 4 show bigger differences. This is always true for all the three runs presented in the study (see Figures S1c and S4c in Supporting Information S1). However, this phenomenon is not observed for the downward FACs (see Figure 4d and Figures S1d and S4d in Supporting Information S1): instead, the FACs in the dawnside sectors 3 and 4 (or duskside sectors 1 and 2) evolve in a quite similar way. As a whole, the day-night asymmetry (or the dawn-dusk asymmetry) is more prominent for upward (or downward) ionospheric FACs. Second, the downward FACs tend to respond more quickly than the upward ones in the corresponding sector. The difference between the upward and downward FACs may be explained as follows. As one can see in Figure 3, the downward FACs at higher latitudes are magnetically connected with the outer magnetosphere and magnetospheric boundaries such as the magnetopause, which are supposed to be affected earlier than the inner magnetosphere by the solar wind discontinuity. By comparison, the upward FACs are more likely linked to the plasma flows in the middle magnetosphere, which is further validated by the fact that the inner magnetosphere tends to respond more slowly than the outer magnetosphere as shown in Figure 4.

Figure 6a and Table S1 in Supporting Information S1 list the response time of the ionosphere to the discontinuity for the three runs. Here, T0 represents the time lag between the time at which the IMF discontinuity encounters the bow shock and the time when the MI system starts to experience perturbations (see Figure 5a). T1, which is always larger than the corresponding T0, is the time delay between the encounter of the discontinuity with the bow shock and the time when the MI system starts to significantly respond. Because of the complexities of the interaction between the discontinuity and the magnetosheath and the follow-on magnetopause, the uncertainty of the onset time of the encounter with the magnetopause is quite large. Thus, here we set the time when the discontinuity encounters the bow shock as the reference time. Selection of this reference time does not really affect our discussion or conclusions, since we mainly focus on the relative values rather than the absolute ones.

On a statistical basis of the three runs as listed in Table S1 of Supporting Information S1 and Figure 6b, the time delays T1 between the encounter of the discontinuity with the bow shock and when the FACs start to significantly respond, are on average ∼1 hr longer for the upward FACs than for the downward ones for Runs 1 and 2, or ∼3 hr longer for Run 3. This time difference is particularly prominent for the dayside ionosphere, that is, sectors 1 and 4. However, the arrival time of the initial perturbations as labeled by T0 is about 20 min earlier for the upward FACs than for the downward ones. This may be explained by the different paths for the waves propagation: perpendicular to the field lines via fast magnetosonic waves or along the field lines via Alfvén waves. For the simulated magnetosphere presented in this study, Alfvén waves take about 80 min to propagate along field lines from the dayside magnetopause to the ionosphere at 1 R_J, while the fast wave may take about 60 min to transversely propagate from the dayside magnetopause to regions near $r = 10\ R_J$. For the upward FACs, the time delays between the time of their significant change and the encounter of the bow shock and the discontinuity are more than 5 hr for all three runs.

3.2.3. Magnetospheric Response

As shown in Figures 4e–4h and 5c–5f, the response of the magnetosphere to the IMF discontinuity shows significant local time asymmetries as well. At the early stage, especially within 10 hr after 00:00 UT, the magnetospheric perturbations in the dayside sectors 1 and 4 (or nightside sectors 2 and 3) are quite similar, indicating that the day-night asymmetry is more prominent for the initial fluctuation which is likely caused by MHD waves in the magnetosphere. As expected, the dayside magnetosphere (sectors 1 and 4) starts to significantly respond earlier than the nightside (sectors 2 and 3). Besides the local time asymmetries, the magnetospheric response is dependent on radial distances to Jupiter. Namely, the outer magnetosphere, particularly in the dayside sectors, tends to respond faster than the inner magnetosphere (see shadings in Figures 4 and 5).

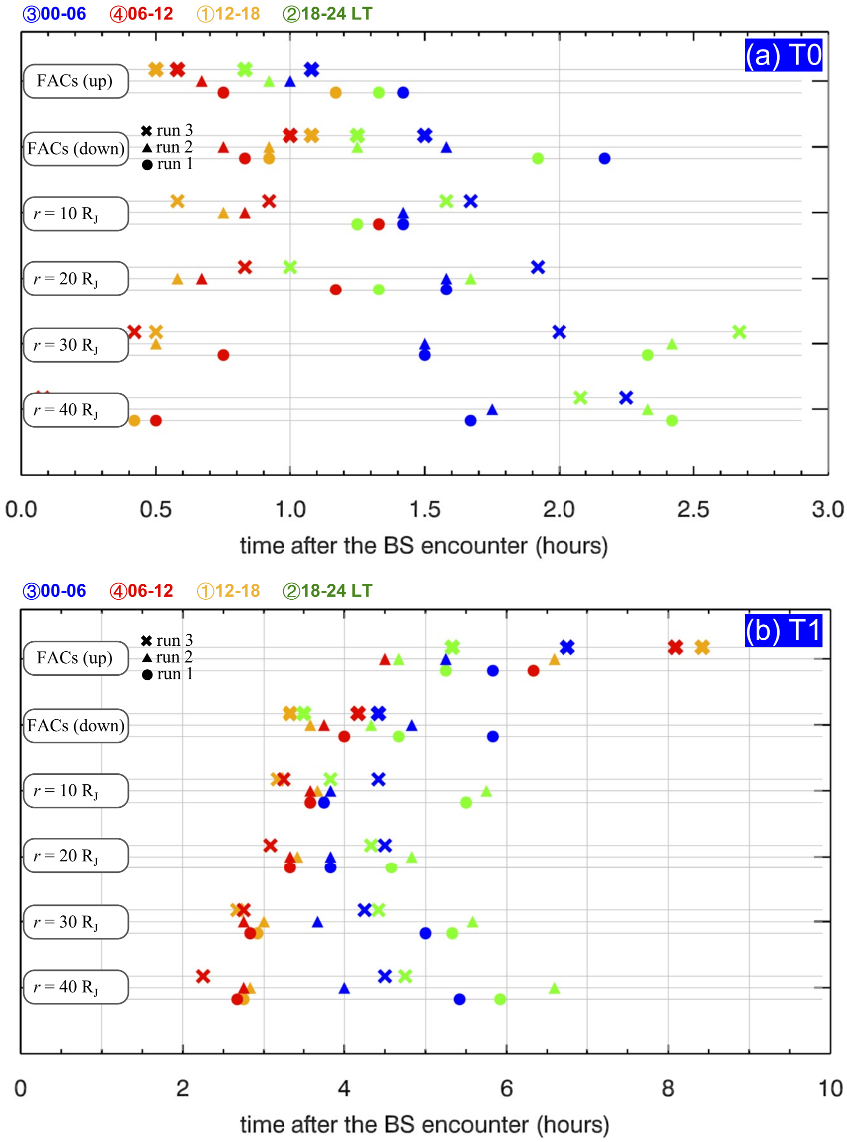

Figure 6. Distribution of the response time (a) T0 and (b) T1 of the magnetosphere-ionosphere system at different sectors and radial distances to the IMF discontinuity for the three runs. The colors represent the four sectors with the same definitions as in Figure 4. The results from the three runs are illustrated with different symbols and are guided by the three horizontal gray lines.

Figure 7 shows the evolution of the magnetosphere for Run 1 as functions of simulation time and radial distances (see Figures S3 and S6 in Supporting Information S1 for Runs 2 and 3, respectively). Similar to Figures 4 and 5, the residual thermal pressure, calculated by subtracting the initial values at 00:00 UT, is set as a proxy reflecting the response of the magnetosphere. The initial thermal pressure is about 0.2 and 0.02 nPa at 6 R_J and 40 R_J, respectively. There seems to be a "pulse" enhancement for nearly all distances within 40 R_J at about 10:00 UT (10 hr) in the dayside magnetosphere, that is, sectors 1 and 4 (see Figures 7a and 7d). As for sectors 1, 2, and 4 (Figures 7a, 7b, and 7d), there appears a separatrix near 15 R_J for sector 1, near 23 R_J for sectors 2 and 4, across which the value of the residual pressure changes sign. In other words, the plasma thermal pressure decreases below the initial value inside of the separatrix, while in the outer magnetosphere outside the separatrix, it increases above its initial state. However, for sector 3, that is, 00:00–06:00 LT, the overall evolution of the magnetosphere is significantly different from the ones observed at the other sectors, which could be related to the tailward reconnection regions (see Figure 1a of Y. X. Wang et al. [2018]).

10.1029/2021JA030207

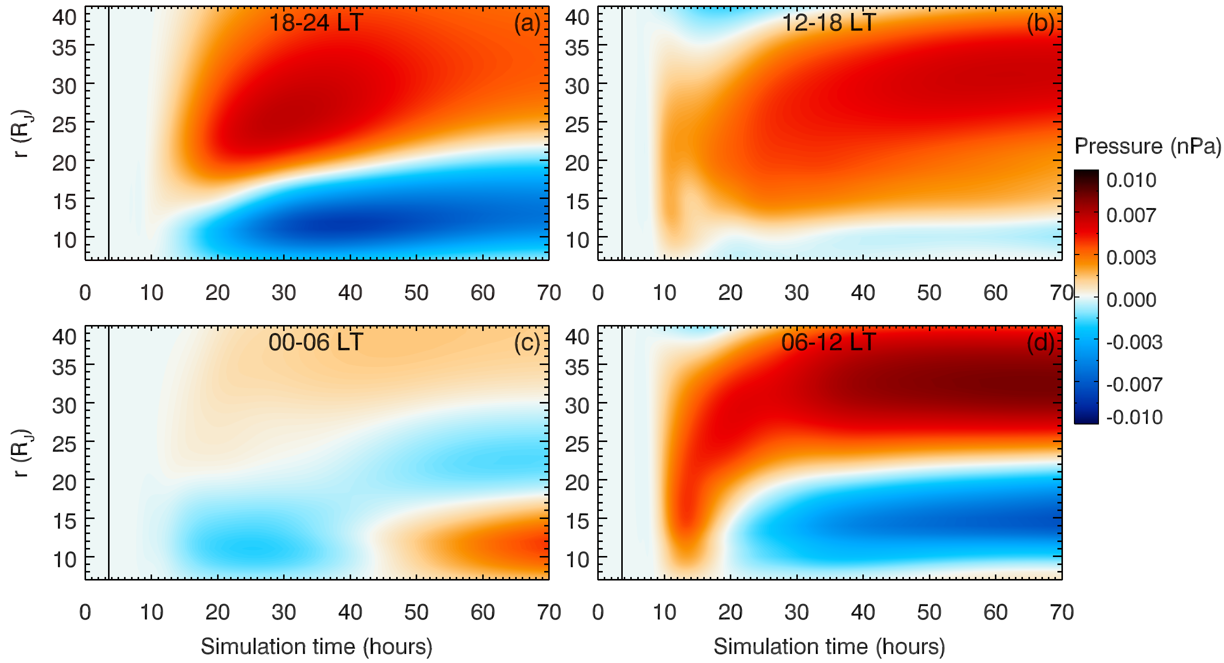

Figure 7. Distribution of the residual pressure relative to the initial state of the magnetosphere as a function of simulation time and radial distances for Run 1 at four sectors: (a) 18:00–24:00 LT, (b) 12:00–18:00 LT, (c) 00:00–06:00 LT, and (d) 06:00–12:00 LT. The black vertical solid lines in each panel indicate the time when the discontinuity encounters the bow shock.

Figure 6 and Tables S1 and S2 in Supporting Information S1 organize the response time of the magnetosphere and the ionosphere in different sectors and at different distances to the IMF discontinuity for the three runs. From this table, we confirm that the dayside magnetosphere (Sectors 1 and 4) responds earlier than the nightside by less than 1 hr for the initial perturbations and several hours for significant changes. The differences in time delays between the perturbations at different distances are less than 1 hr, which is consistent with the magnetosonic waves propagation time. The outer magnetosphere seems to responds more quickly than the inner magnetosphere on the dayside, while it is not true for the nightside sectors 2 and 3. This may be explained by the time sequence of the effects of the solar wind discontinuity. The perturbations originating in the solar wind propagate through the magnetosheath and dayside outer magnetosphere to the inner magnetosphere in the form of Alfvén waves along the magnetic field lines and/or of fast magnetosonic waves transverse to the magnetic field.

4. Discussion

4.1. Comparison With Simulations and Observations at Earth

The dynamics of the terrestrial MI system is mainly controlled by the solar wind. At Earth, the response of the MI system to the solar wind along with the IMF has been widely studied via observational data and simulations (e.g., Yu & Ridley, 2009 and references therein; Tenfjord et al., 2017; C. Wang et al., 2013). Yu and Ridley (2009) modeled a north-to-south IMF discontinuity interacting with an initial magnetosphere under northward IMF, which corresponds to a closed magnetosphere at Earth. They found that the time it takes for the ionosphere to significantly respond to this discontinuity from the encounter of the IMF transition with the bow shock varies with the solar wind speed, ranging from nearly 15 min (min) for a solar wind speed of 300 km/s to ~6 min for solar wind speeds of 600 km/s. Besides, the IMF transition takes about 3–9 min to propagate from the bow shock to the subsolar magnetopause for solar wind speeds of 300–600 km/s. A delay time of 7–8 min for the IMF orientation to have effects on the ionosphere after it hits the bow shock was reported through simulations and observations (Lu et al., 2002; Ridley et al., 1998; Slinker et al., 2001). However, it is widely accepted that the ionosphere responds globally to a sudden southward turning of IMF nearly simultaneously with no significant day-night difference in time (Yu & Ridley, 2009 and references therein). Using in situ magnetic field measurements, Tenfjord et al. (2017) found that the Earth's magnetosphere at geosynchronous distances responds to a change in IMF-By in less than 15 min at all local times from the bow shock arrival time, while the reconfiguration time is less than 46 min.

In the case of Jupiter, things are quite different. First, the time for the MI system to respond to the IMF discontinuity after its encounter with the bow shock spans from ∼2 to ∼8 hr, depending on solar wind conditions, local times, radial distances, and the initial magnetospheric states. The reconfiguration time, which is defined as the time it takes to reach the final state of the magnetosphere, is approximated to be over 70 hr (see Figures 4c–4h). As a result, the timescales for the Jovian MI system to respond to the IMF rotation and the magnetospheric reconfiguration are, respectively, on average 20 and 90 times longer than the corresponding times at Earth. The IMF transition takes about 1.5 hr for the propagation from the bow shock to the subsolar magnetopause for run 1, which is much larger than the 5.3 min at Earth for a north-to-south discontinuity with the same solar wind speed of 400 km/s (Yu & Ridley, 2009).

Second, the Jovian MI system displays strong local time asymmetries in its response to the IMF discontinuity. For example, the dayside ionospheric FACs tend to respond more quickly than the nightside ones by over 30 min (compare sectors 1 and 2 for run 1 in Table S1 of Supporting Information S1). Such day-night asymmetry is always observed for all local times in the three runs presented in this study.

Finally, in addition to the day-night asymmetry, the downward FACs are found to respond earlier than the upward ones by a time ranging from less than 1 hr to several hours (see Table S1 in Supporting Information S1), which is more prominent in the dayside ionosphere.

4.2. Implications From the Main Oval Morphology

The UV main ovals observed by Hubble Space Telescope (HST, Clarke et al., 1998; Gérard et al., 2014) and Juno (Gladstone et al., 2017) shows strong north-south asymmetry and their general morphologies are consistent with the planetary magnetic field (Connerney et al., 2018). This is not surprising since precipitating electrons are always guided by the local magnetic field.

As presented in Section 3.1, the general morphology of the simulated upward ionospheric FACs obtained from our MHD model agrees quite well with that of the main auroral ovals in both northern and southern poles when we use the JRM09 model for the MI mapping (see Figure 2). This very good matching between the simulated upward FACs and the observed main ovals confirms that the simulated upward FACs obtained from MHD models could be used as a first order proxy for the general morphology of main auroral ovals.

The simulated ionospheric upward FACs obtained from the dipole mapping method (see Figures 3a and 3b) are distributed between 12° and 19° magnetic latitudes with a peak at around 15°, which magnetically map to the equatorial magnetospheric regions ranging from ∼10 to 30 R_J for the dayside, and even much farther for the nightside due to the more elongated magnetic field lines in the tailward magnetosphere. These results, to some extent, are consistent with the corotation enforcement theory (Cowley & Bunce, 2001) as described in Section 3.1 with regard to the upward FACs and the main auroral oval.

However, as described in Section 1.2, the corotation enforcement theory has been challenged by some observations (Bonfond et al., 2020), and the links between the main oval and the upward ionospheric FACs are not always firm or reliable. Despite the absence of a deterministic relationship between the upward FACs and the main oval, they could be correlated in some cases. The Jovian UV aurora is generated by the precipitating electrons impacting with the atmosphere (Gérard et al., 2014), and these downward electron populations as charge carriers contribute to the upward FACs. As a result, the main oval and the related electron precipitations are more likely to be within the upward FACs, although these accelerated downward moving electrons could be also related to the downward FACs or even "zero FACs" regions (Mauk et al., 2018, 2020).

4.3. Directions for Future Work

The main focus of this study is on the interaction of the idealized IMF rotation with a quasi-steady and highly compressed magnetosphere. We found that the response of the MI system to IMF rotations differs greatly for different solar wind conditions and the associated magnetospheric states (comparing runs 1 and 3). It is likely that the related response time of the MI system to the solar wind tends to increase for a larger and closed magnetosphere. Thus, in order to further understand the response of the Jovian MI system to the solar wind and IMF, more simulations under different solar wind conditions or more realistic solar wind provided by in situ observations (e.g., Wilson et al., 2018) or heliospheric models (e.g., Y. X. Wang et al., 2020) are needed.

Second, as mentioned in Section 2.2, this work is as a first attempt to examine the effects of a realistic Jovian magnetic field on the morphology of the upward ionospheric FACs. However, this realistic magnetic field is not explicitly included in the MHD calculation cycle (see Figure 2) but is only used to derive the ionosphere FACs by mapping from the magnetosphere to the ionosphere. The implementation of this realistic magnetic field, including a tilt angle relative to the rotational axis, the strong nondipole components, and the magnetic anomaly particularly at the north pole should be addressed in a future study. In such a situation, dayside reconnection does not occur at the subsolar point but varies with time due to the rotating tilted Jovian magnetic field.

Finally, the ionospheric conductances used in our current model are uniform and time-independent, which does not reflect the realistic case since ionosphere conductances are strongly modulated by particle precipitations and are significantly enhanced within auroral regions (Gérard et al., 2020; Y. X. Wang, Blanc, et al., 2021). A variable and nonuniform distribution of conductances should be considered in future simulations.

5. Summary and Conclusions

In this paper, we have conducted three simulation runs to investigate the response of the MI system at Jupiter to an IMF tangential discontinuity. Compared with preexisting MHD models, we used here the JRM09 model for the derivation of the ionospheric FACs, as a first attempt to examine the effects of the realistic Jovian magnetic field on the shaping of the main oval morphology. This study demonstrates that the timescales for the Jovian MI system to respond to IMF rotations and the magnetospheric reconfiguration are much longer than that of the Earth, and the MI system response is local-time dependent. Such characteristic timescales and features of the MI system responding to the IMF rotations are important and useful for the causal study of the solar wind's interaction with Jovian magnetosphere. For example, these timescales could be used as a reference time to investigate the chain of causality between some specific solar wind transient events and the evolution of the aurora during when the solar wind and aurora imaging data are both available.

The results of this paper can be summarized as follows:

1. The response of the MI system to the IMF discontinuity shows significant local time asymmetries in terms of both magnitudes and general trends.
   At the ionospheric level, the duskside FACs are anticorrelated with the dawnside ones at the early stage of the simulation before ~20:00 UT. In addition, the responses of the upward and downward FACs are significantly different. For instance, the day-night asymmetry is more prominent for upward FACs, while for downward FACs, the dawn-dusk asymmetry is more evident. Besides, as expected, the dayside magnetosphere starts to significantly respond at an earlier time than the nightside sectors.
2. The magnetospheric response to the IMF rotation varies with radial distances to Jupiter. The outer magnetosphere seems to responds more quickly than the inner magnetosphere on the dayside, while it is not clear for the nightside sectors.
3. The magnetosphere and ionosphere significantly respond to the IMF discontinuities in ~2–6 and ~3–8 hr from the arrival at the bow shock, depending on local times and radial distances.
4. The simulated ionospheric upward FACs agree well with the observed main oval for both hemispheres when we use the JRM09 model to map the FACs from the inner boundary of our MHD model to the ionosphere. This confirms that the planetary magnetic field greatly shapes the ionospheric FACs as well as the main auroral emissions. Their mutual consistency implies that the simulated upward FACs could be used as a first order proxy for the general morphology of main ovals.

Data Availability Statement

All the simulation data along with the program for reading are available at National Space Science Data Center (https://dx.doi.org/10.12176/01.99.02056) as shown in the in-text data citation reference: Y. X. Wang, Guo, et al. (2021).

Acknowledgments

This work was supported by the Strategic Priority Research Program of Chinese Academy of Sciences Grant No. XDB 41000000, QYZDJ-SSW-JSC028, NNSFC grants 42150105, 41874171, and 41731070, and in part by the Specialized Research Fund for State Key Laboratories of China.

References

Badman, S. V., Bonfond, B., Fujimoto, M., Gray, R. L., Kasaba, Y., Kasahara, S., et al. (2016). Weakening of Jupiter's main auroral emission during January 2014. *Geophysical Research Letters*, *43*(3), 988–997. https://doi.org/10.1002/2015gl067366

Bagenal, F., Adriani, A., Allegrini, F., Bolton, S. J., Bonfond, B., Bunce, E. J., et al. (2017). Magnetospheric science objectives of the Juno mission. *Space Science Reviews*, *213*(1–4), 219–287. https://doi.org/10.1007/s11214-014-0036-8

Bonfond, B., Grodent, D., Gérard, J.-C., Stallard, T., Clarke, J. T., Yoneda, M., et al. (2012). Auroral evidence of Io's control over the magnetosphere of Jupiter. *Geophysical Research Letters*, *39*, L01105. https://doi.org/10.1029/2011GL050253

Bonfond, B., Yao, Z., & Grodent, D. (2020). Six pieces of evidence against the corotation enforcement theory to explain the main aurora at Jupiter. *Journal of Geophysical Research: Space Physics*, *125*(11). https://doi.org/10.1029/2020ja028152

Chané, E., Saur, J., Keppens, R., & Poedts, S. (2017). How is the Jovian main auroral emission affected by the solar wind? *Journal of Geophysical Research: Space Physics*, *122*(2), 1960–1978. https://doi.org/10.1002/2016ja023318

Chané, E., Saur, J., & Poedts, S. (2013). Modeling Jupiter's magnetosphere: Influence of the internal sources. *Journal of Geophysical Research: Space Physics*, *118*(5), 2157–2172. https://doi.org/10.1002/jgra.50258

Clarke, J. T., Ballester, G., Trauger, J., Ajello, J., Pryor, W., Tobiska, K., et al. (1998). Hubble Space Telescope imaging of Jupiter's UV aurora during the Galileo orbiter mission. *Journal of Geophysical Research*, *103*(E9), 20217–20236. https://doi.org/10.1029/98je01130

Clarke, J. T., Nichols, J., Gérard, J.-C., Grodent, D., Hansen, K. C., Kurth, W., et al. (2009). Response of Jupiter's and Saturn's auroral activity to the solar wind. *Journal of Geophysical Research*, *114*(A5). https://doi.org/10.1029/2008ja013694

Connerney, J. E. P., Kotsiaros, S., Oliversen, R. J., Espley, J. R., Joergensen, J. L., Joergensen, P. S., et al. (2018). A new model of Jupiter's magnetic field from Juno's first nine orbits. *Geophysical Research Letters*, *45*(6), 2590–2596. https://doi.org/10.1002/2018GL077312

Cowley, S. W. H., & Bunce, E. J. (2001). Origin of the main auroral oval in Jupiter's coupled magnetosphere–ionosphere system. *Planetary and Space Science*, *49*(10–11), 1067–1088. https://doi.org/10.1016/s0032-0633(00)00167-7

Delamere, P. A., Bagenal, F., Paranicas, C., Masters, A., Radioti, A., Bonfond, B., et al. (2015). Solar wind and internally driven dynamics: Influences on magnetodiscs and auroral responses. *Space Science Reviews*, *187*(1–4), 51–97. https://doi.org/10.1007/978-1-4939-3395-2_4

Dunn, W. R., Branduardi-Raymont, G., Elsner, R. F., Vogt, M. F., Lamy, L., Ford, P. G., et al. (2016). The impact of an ICME on the Jovian X-ray aurora. *Journal of Geophysical Research: Space Physics*, *121*(3), 2274–2307. https://doi.org/10.1002/2015ja021888

Dunn, W. R., Gray, R., Wibisono, A. D., Lamy, L., Louis, C., Badman, S. V., et al. (2020). Comparisons between Jupiter's X-ray, UV and radio emissions and in-situ solar wind measurements during 2007. *Journal of Geophysical Research: Space Physics*, *125*(6). https://doi.org/10.1029/2019ja027222

Fukazawa, K., Ogino, T., & Walker, R. J. (2005). Dynamics of the Jovian magnetosphere for northward interplanetary magnetic field (IMF). *Geophysical Research Letters*, *32*(L03), 202. https://doi.org/10.1029/2004GL021392

Fukazawa, K., Ogino, T., & Walker, R. J. (2006). Configuration and dynamics of the Jovian magnetosphere. *Journal of Geophysical Research*, *111*(A10), A10207. https://doi.org/10.1029/2006ja011874

Gérard, J.-C., Bonfond, B., Grodent, D., Radioti, A., Clarke, J. T., Gladstone, G. R., et al. (2014). Mapping the electron energy in Jupiter's aurora: Hubble spectral observations. *Journal of Geophysical Research: Space Physics*, *119*(11), 9072–9088. https://doi.org/10.1002/2014ja020514

Gérard, J.-C., Gkouvelis, L., Bonfond, B., Grodent, D., Gladstone, G. R., Hue, V., et al. (2020). Spatial distribution of the Pedersen conductance in the Jovian aurora from Juno-UVS spectral images. *Journal of Geophysical Research: Space Physics*, *125*(8). https://doi.org/10.1029/2020ja028142

Gladstone, G. R., Persyn, S. C., Eterno, J. S., Walther, B. C., Slater, D. C., Davis, M. W., et al. (2017). The ultraviolet spectrograph on NASA's Juno mission. *Space Science Reviews*, *213*(1–4), 447–473. https://doi.org/10.1007/s11214-014-0040-z

Grodent, D., Bonfond, B., Yao, Z., Gérard, J.-C., Radioti, A., Dumont, M., et al. (2018). Jupiter's aurora observed with HST during Juno orbits 3 to 7. *Journal of Geophysical Research: Space Physics*, *123*(5), 3299–3319. https://doi.org/10.1002/2017ja025046

Hill, T. W. (2001). The Jovian auroral oval. *Journal of Geophysical Research*, *106*(A5), 8101–8107. https://doi.org/10.1029/2000ja000302

Joy, S. P., Kivelson, M. G., Walker, R. J., Khurana, K. K., Russell, C. T., & Ogino, T. (2002). Probabilistic models of the Jovian magnetopause and bow shock locations. *Journal of Geophysical Research*, *107*(A10), 1309. https://doi.org/10.1029/2001JA009146

Khurana, K. K., Kivelson, M. G., Vasyliunas, V. M., Krupp, N., Woch, J., Lagg, A., et al. (2004). The configuration of Jupiter's magnetosphere. In F. Bagenal, T. E. Dowling, & W. B. Mckinnon (Eds.), *Jupiter: The planet, satellites and magnetosphere* (pp. 593–616). Cambridge University Press.

Kotsiaros, S., Connerney, J. E. P., Clark, G., Allegrini, F., Gladstone, G. R., Kurth, W. S., et al. (2019). Birkeland currents in Jupiter's magnetosphere observed by the polar-orbiting Juno spacecraft. *Nature Astronomy*, *3*(10), 904–909. https://doi.org/10.1038/s41550-019-0819-7

Krupp, N., Vasyliunas, V. M., Woch, J., Lagg, A., Khurana, K. K., Kivelson, M. G., et al. (2004). Dynamics of the Jovian magnetosphere. In F. Bagenal, T. E. Dowling, & W. B. Mckinnon (Eds.), *Jupiter: The planet, satellites and magnetosphere* (pp. 617–638). Cambridge University Press.

Lu, G., Holzer, T. E., Lummerzheim, D., Ruohoniemi, J. M., Stauning, P., Troshichev, O., et al. (2002). Ionospheric response to the interplanetary magnetic field southward turning: Fast onset and slow reconfiguration. *Journal of Geophysical Research*, *107*(A8), SIA 2-1–SIA 2-9. https://doi.org/10.1029/2001ja000324

Mauk, B. H., Clark, G., Gladstone, G. R., Kotsiaros, S., Adriani, A., Allegrini, F., et al. (2020). Energetic particles and acceleration regions over Jupiter's polar cap and main aurora: A broad overview. *Journal of Geophysical Research: Space Physics*, *125*(3), e2019JA027699. https://doi.org/10.1029/2019ja027699

Mauk, B. H., Haggerty, D. K., Paranicas, C., Clark, G., Kollmann, P., Rymer, A. M., et al. (2018). Diverse electron and ion acceleration characteristics observed over Jupiter's main aurora. *Geophysical Research Letters*, *45*(3), 1277–1285. https://doi.org/10.1002/2017GL076901

Nichols, J. D., & Cowley, S. W. H. (2004). Magnetosphere-ionosphere coupling currents in Jupiter's middle magnetosphere: Effect of precipitation-induced enhancement of the ionospheric Pedersen conductivity. *Annales Geophysicae*, *22*(5), 1799–1827. https://doi.org/10.5194/angeo-22-1799-2004

Radioti, A., Gérard, J. C., Grodent, D., Bonfond, B., Krupp, N., & Woch, J. (2008). Discontinuity in Jupiter's main auroral oval. *Journal of Geophysical Research-Space Physics*, *113*(A1). https://doi.org/10.1029/2007ja012610

Ridley, A. J., Lu, G., Clauer, C. R., & Papitashvili, V. O. (1998). A statistical study of the ionospheric convection response to changing interplanetary magnetic field conditions using the assimilative mapping of ionospheric electrodynamics technique. *Journal of Geophysical Research*, *103*(A3), 4023–4039. https://doi.org/10.1029/97ja03328

Sarkango, Y., Jia, X., & Toth, G. (2019). Global MHD simulations of the response of Jupiter's magnetosphere and ionosphere to changes in the solar wind and IMF. *Journal of Geophysical Research: Space Physics*, *124*(7), 5317–5341. https://doi.org/10.1029/2019ja026787

Slinker, S. P., Fedder, J. A., Ruohoniemi, J. M., & Lyon, J. G. (2001). Global MHD simulation of the magnetosphere for November 24, 1996. *Journal of Geophysical Research*, *106*(A1), 361–380. https://doi.org/10.1029/2000ja000603

Southwood, D. J., & Kivelson, M. G. (2001). A new perspective concerning the influence of the solar wind on the Jovian magnetosphere. *Journal of Geophysical Research*, *106*(A4), 6123–6130. https://doi.org/10.1029/2000ja000236

Tanaka, T., Ebihara, Y., Watanabe, M., Fujita, S., & Kataoka, R. (2021). Global simulation of the Jovian magnetosphere: Transitional structure from the Io plasma disk to the plasma sheet. *Journal of Geophysical Research: Space Physics*, *126*(6). https://doi.org/10.1029/2021ja029232

Tenfjord, P., Østgaard, N., Strangeway, R., Haaland, S., Snekvik, K., Laundal, K. M., et al. (2017). Magnetospheric response and reconfiguration times following IMF B_y reversals. *Journal of Geophysical Research: Space Physics*, *122*(1), 417–431. https://doi.org/10.1002/2016ja023018

Vogt, M. F., Kivelson, M. G., Khurana, K. K., Walker, R. J., Bonfond, B., Grodent, D., & Radioti, A. (2011). Improved mapping of Jupiter's auroral features to magnetospheric sources. *Journal of Geophysical Research*, *116*(A3). https://doi.org/10.1029/2010ja016148

Wang, C., Guo, X. C., Peng, Z., Tang, B. B., Sun, T. R., Li, W. Y., & Hu, Y. Q. (2013). Magnetohydrodynamics (MHD) numerical simulations on the interaction of the solar wind with the magnetosphere: A review. *Science China Earth Sciences*, *56*(7), 1141–1157. https://doi.org/10.1007/s11430-013-4608-3

Wang, Y. X., Blanc, M., Louis, C., Wang, C., André, N., Adriani, A., et al. (2021). A preliminary study of magnetosphere-ionosphere-thermosphere coupling at Jupiter: Juno multi-instrument measurements and modeling tools. *Journal of Geophysical Research: Space Physics*, *126*(9). https://doi.org/10.1029/2021ja029469

Wang, Y. X., Guo, X., Tang, B., Li, W., & Wang, C. (2018). Modeling the Jovian magnetosphere under an antiparallel interplanetary magnetic field from a global MHD simulation. *Earth and Planetary Physics*, *2*(4), 303–309. https://doi.org/10.26464/epp2018028

Wang, Y. X., Guo, X., Wang, C., & Blanc, M. (2021). Simulation data of "response of the Jovian magnetosphere-ionosphere system to the interplanetary magnetic field discontinuity: A simulation study". *V1. NSSDC Space Science Article Data Repository*. https://doi.org/10.12176/01.99.02056

Wang, Y. X., Guo, X. C., Wang, C., Florinski, V., Shen, F., Li, H., & Blanc, M. (2020). MHD modeling of the background solar wind in the inner heliosphere from 0.1 to 5.5 AU: Comparison with in-situ observations. *Space Weather*, *18*(6). https://doi.org/10.1029/2019sw002262

Wilson, R. J., Bagenal, F., Valek, P. W., McComas, D. J., Allegrini, F., Ebert, R. W., et al. (2018). Solar wind properties during Juno's approach to Jupiter: Data analysis and resulting plasma properties utilizing a 1-D forward model. *Journal of Geophysical Research: Space Physics*, *123*(4), 2772–2786. https://doi.org/10.1002/2017JA024860

Yu, Y., & Ridley, A. J. (2009). Response of the magnetosphere-ionosphere system to a sudden southward turning of interplanetary magnetic field: Response to a sudden southward turning OF IMF. *Journal of Geophysical Research*, *114*(A3). https://doi.org/10.1029/2008ja013292

Zhang, B., Delamere, P. A., Ma, X., Burkholder, B., Wiltberger, M., Lyon, J. G., et al. (2018). Asymmetric Kelvin-Helmholtz instability at Jupiter's magnetopause boundary: Implications for corotation-dominated systems. *Geophysical Research Letters*, *45*(1), 56–63. https://doi.org/10.1002/2017gl076315

Zhang, B., Delamere, P. A., Yao, Z., Bonfond, B., Lin, D., Sorathia, K. A., et al. (2021). How Jupiter's unusual magnetospheric topology structures its aurora. *Science Advances*, *7*(15), eabd1204. https://doi.org/10.1126/sciadv.abd1204